LASER INTERFEROMETER GRAVITATIONAL WAVE OBSERVATORY
- LIGO -
CALIFORNIA INSTITUTE OF TECHNOLOGY
MASSACHUSETTS INSTITUTE OF TECHNOLOGY

Technical Note	**LIGO-T1700275-v5**	2017/09/21

Final Report: Finite Element Modeling of the electrostatic drive for C.Ri.Me. lab

Zachary Rose — Mentor Gabriele Vajente

Distribution of this document:

LIGO Scientific Collaboration

California Institute of Technology
LIGO Project, MS 18-34
Pasadena, CA 91125
Phone (626) 395-2129
Fax (626) 304-9834
E-mail: info@ligo.caltech.edu

Massachusetts Institute of Technology
LIGO Project, Room NW17-161
Cambridge, MA 02139
Phone (617) 253-4824
Fax (617) 253-7014
E-mail: info@ligo.mit.edu

LIGO Hanford Observatory
Route 10, Mile Marker 2
Richland, WA 99352
Phone (509) 372-8106
Fax (509) 372-8137
E-mail: info@ligo.caltech.edu

LIGO Livingston Observatory
19100 LIGO Lane
Livingston, LA 70754
Phone (225) 686-3100
Fax (225) 686-7189
E-mail: info@ligo.caltech.edu

http://www.ligo.caltech.edu/

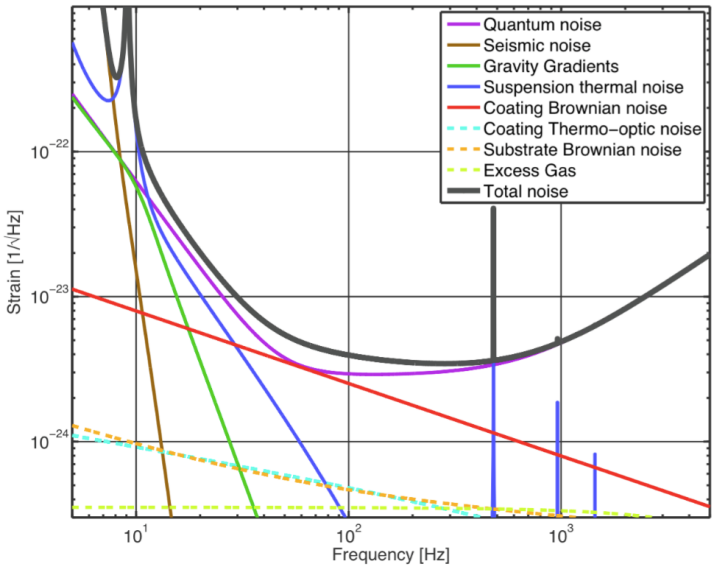

Figure 1: A plot of the various sources of noise at aLIGO from [5]

Abstract

This is the final report for my LIGO SURF program. In this document I will present some background about the Coating Ringdown Measurement Experiment (C.Ri.Me.) Laboratory's purpose and methodology, specifically as it pertains to the use of an electrostatic drive (ESD). I will then describe the working principles of the drive as well as my efforts to model and then improve upon the current design.

1 Introduction

1.1 Theoretical Background

In the most recent interferometric gravitational wave detectors, one of the most substantial displacement noise sources is thermal noise, as can be seen in figure 1. In the frequency range relevant to Advanced LIGO (aLIGO), the mirror coatings are the dominant source of this noise. The available options to limit this thermal noise are increased beam size, thinner coatings, or coatings with a smaller loss angle. Since beam size affects other systems within LIGO and thinner coatings will affect their reflectivity, mirror coatings with a very low loss angle ϕ are extremely desirable.

Reflective coatings are made by alternating materials with high and low refractive indices, the resultant loss angle of the coating is largely determined by the high index material. The overall goal of this experiment is to develop a consistent and effective method to calculate the loss angle ϕ of the reflective coatings on a silica substrate. This is accomplished by calculating the Q factors of a silica sample both before and after reflective coatings are applied, which boils down to understanding the exponential decay, or ringdown, of the disks' resonant modes. After excitation the disk can

be considered as a damped harmonic oscillator, so exponential decays are to be expected. The mechanical quality factor can be calculated by

$$Q = 2\pi \frac{E_{tot}}{\Delta E_{cycle}} \tag{1}$$

where E_{tot} is the total energy in a given mode and ΔE_{cycle} is the energy dispersed per cycle. The loss angle ϕ is the reciprocal of Q. Once the coating has been applied, the loss angle of the coating can be extracted from the fact that

$$\phi = \frac{\phi_{substrate} E_{substrate} + \phi_{coating} E_{coating}}{E_{tot}} [5] \tag{2}$$

where ϕ is the loss angle for the coated sample, $\phi_{substrate}$ is the loss angle extracted from the ringdown of the uncoated sample, $E_{substrate}$ is the elastic energy in the silica disk, $\phi_{coating}$ is the loss angle of the reflective coating, and $E_{coating}$ is the elastic energy in the reflective coating.

1.2 Experimental Setup

A simplified scheme of the experimental setup can be seen in figure 2 and consists of a gently suspended sample [1], an optical lever, and an electrostatic drive. The modes of the silica sample are excited through the use of an actuator similar to the one in figure 3; the current model has different electrode sizing and spacing. Each fundamental mode is identified and tracked using python and MATLAB scripts and the resultant decay data is used to calculate their Q factors.

As diagrammed in figure 2, the sample, a 1 mm thick disk with a radius of 75 mm, is balanced on top of a half-spherical lens made of silicon [1]. This is called gentle nodal suspension and it is utilized to minimize coupling between the sample and its suspension mechanism to ensure accuracy. Due to the small contact radius at a nodal point of the sample, very little energy is coupled into the suspension mechanism. This method is also useful because it is relatively easy to setup and repeat.

The vibrational modes of the disk are measured with an optical lever. The lever is equipped with a quadrant photodiode which allows it to accurately measure the surface motion of the sample. The ESD that excites the disk consists of two interlocking combs of electrodes as in figure 3, one of which is maintained at ground potential while the other is driven with a time varying voltage. The electric field created by this actuator induces and interacts with dipoles in the silica which results in a net force on the disk as in figure 4.

Figure 2: A simple diagram of the experimental setup from [5]

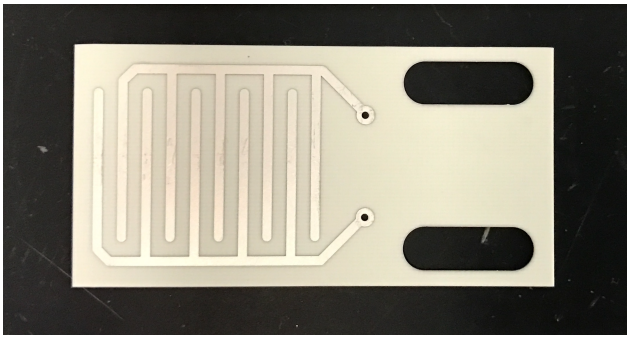

Figure 3: An older model of the electrostatic actuator that excites the samples from [3]

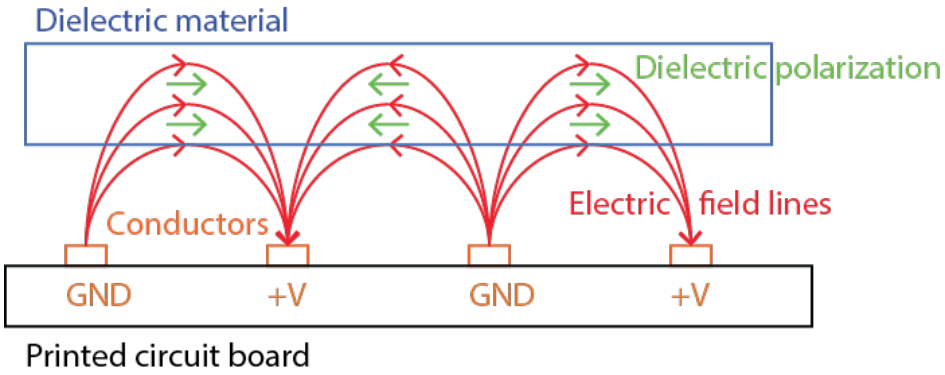

Figure 4: A diagram of the interaction between the actuator and sample from [5]

2 My Project

2.1 Problem Statement

In order to calculate Q factors, the ringdown of all of the fundamental modes of the disk must be recorded. To improve accuracy, it is important that the ESD excites all of the fundamental modes of the sample with the largest possible amplitude. The goal of my project is to determine the optimal shape of the electrostatic actuator to drive all of the fundamental vibrational modes maximally. An older actuator design can be seen in figure 3.

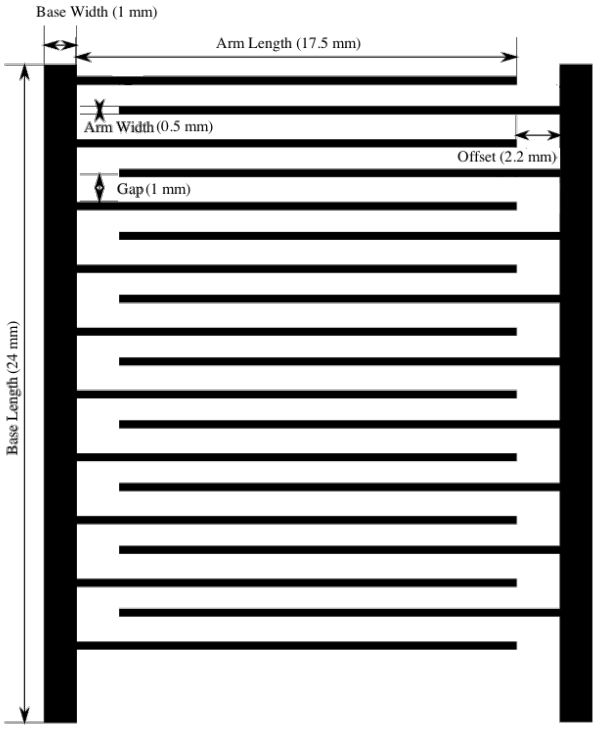

Figure 5: A technical drawing of the ESD with both adjustable parameter names and their original values

2.2 Completed Work

I created a COMSOL model of the current ESD setup to match what existed in the lab. I modeled the actuator by itself as in figure 5, using the parameters in Table 1; the resulting potential and electric fields can be seen in figure 6. In order to confirm that the simulation was physically reasonable I set a potential difference of 1000V for ease of calculations, the electric field at a distance of 1 mm above or next to the actuator is approximately 10^6V/m as expected.

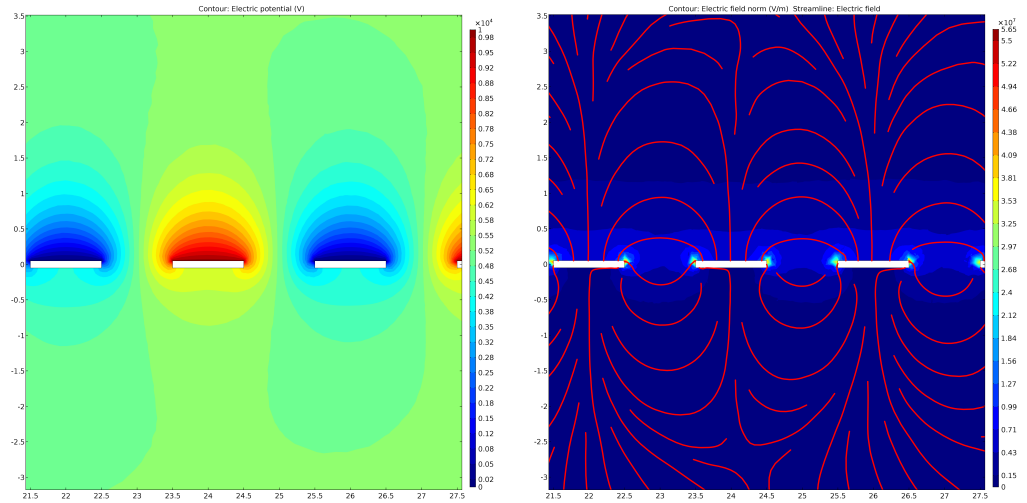

(a) A contour plot of the electric potential (V)

(b) Plot of the E field (V/m) with field lines overlaid in red

Figure 6: Plots of electrostatic quantities in a cross section of the ESD

ESD Parameter	**Value**
Gap	1 mm
Arm width	0.3 mm
Arm length	17.5 mm
Base width	1 mm
Base length	24 mm
Thickness	.1 mm
Number of arms (top)	9
Number of arms (bottom)	10
Sample Parameter	**Value**
Diameter	75 mm
Thickness	1 mm
ESD/Sample separation	1 mm
Relative permittivity (ε_r)	2.09
Density (ρ)	2203 kg/m^3
Young's Modulus (E)	73 GPa
Poisson's ratio (ν)	0.17

Table 1: Electrostatic Drive and Sample Parameters

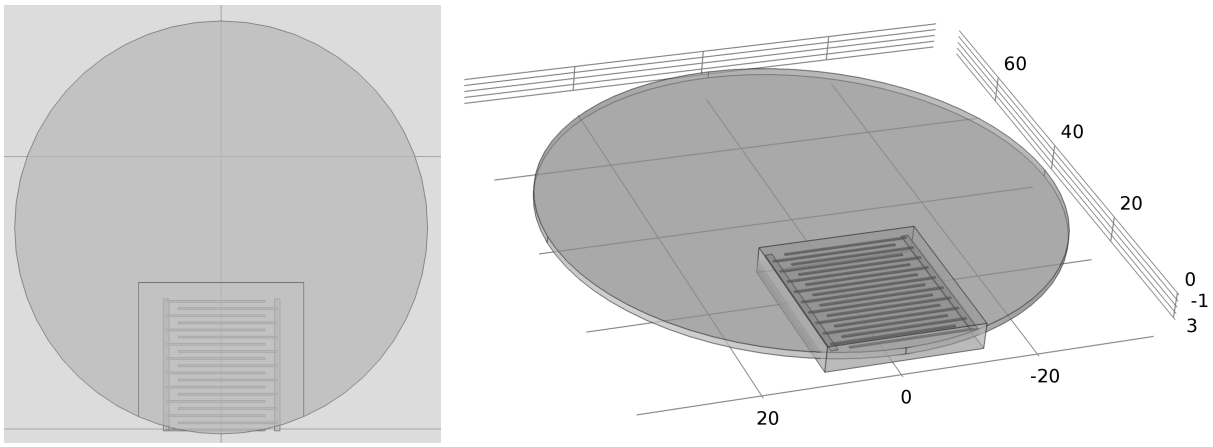

Figure 7: Two views of the COMSOL model geometry, the box surrounding the ESD is used to create a finer mesh in the region immediately surrounding the ESD

The next step was adding in a model of the sample, computing the induced polarization, and calculating a resultant force profile on the sample disk. The geometry of the model was built to match the arrangement in the lab and the technical drawings [8]. The geometry can be seen in figure 7 and the parameters in Table 1. In order to make the results as accurate as possible a fine mesh size is desirable, however the smaller the mesh the more memory intensive the model becomes. To minimize both mesh size and solution time, I created a geometric domain in the region surrounding the ESD and the sample above it, this can be seen in figure 7 as the small box immediately around the ESD. Over the domain near the ESD the mesh is extremely fine, each element is as small as 2.5×10^{-3} mm and no bigger than .25 mm. Over the rest of the domain the mesh is automatically defined at the preset "normal" size. The mesh is so fine the computer cannot fully render images of it as can be seen by the aliasing in the center of figure 8.

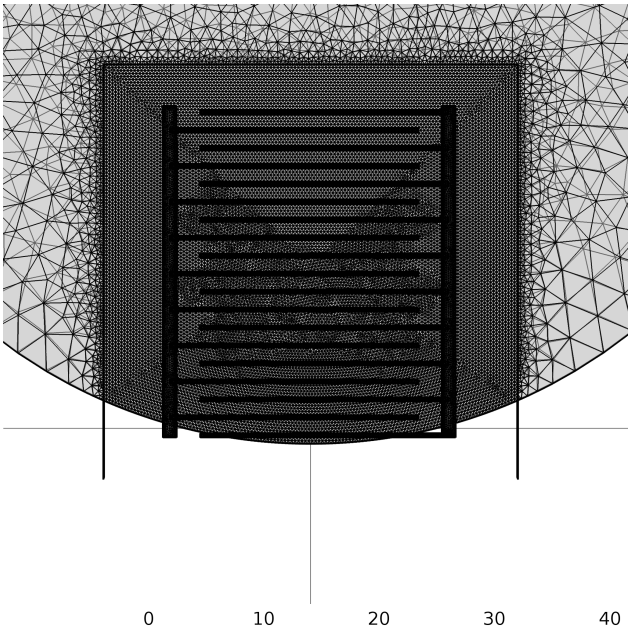

Figure 8: The meshing structure of the model

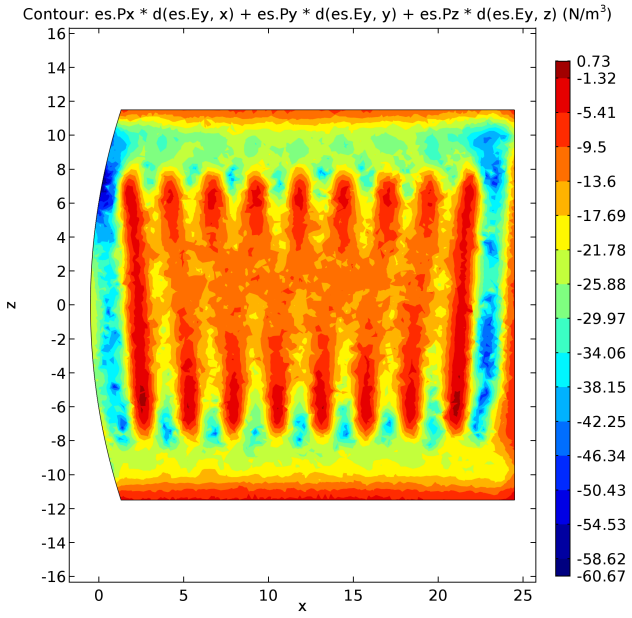

(a) Plot of the force distribution for the $(P \cdot \nabla)E$ case

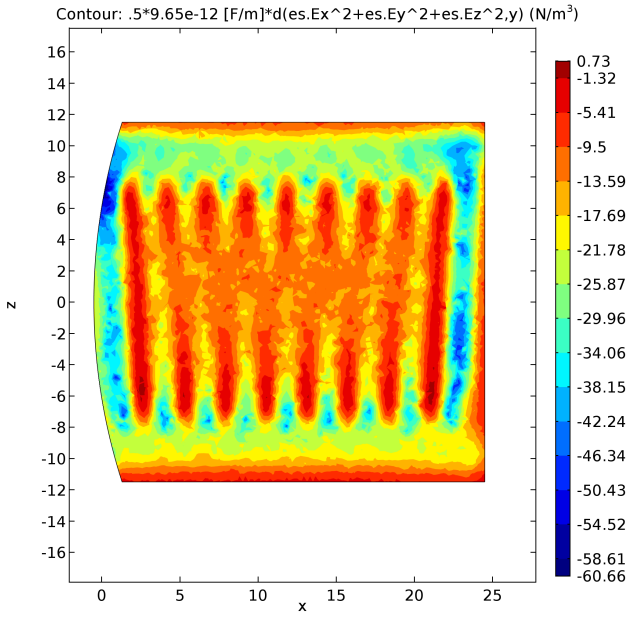

(b) Plot of the force distribution for the $\frac{1}{2}\varepsilon_0\chi_e\nabla\left(E^2\right)$ case

Figure 9: Plots of the force distribution in N/m^3

In addition to matching the lab setup spatially, it is important to confirm the model with as many physical calculations as possible to ensure accuracy to real world effects. Theoretically speaking, the resultant force from induced polarization in a dielectric in an electric field is given by

$$\mathbf{F} = (\mathbf{P} \cdot \nabla)\mathbf{E} \text{ [6]}. \tag{3}$$

Alternatively, the energy density of a dielectric placed in a fixed electric field is

$$U = -\frac{1}{2}\mathbf{P} \cdot \mathbf{E} \text{ [7]}. \tag{4}$$

From this we can derive the force as

$$\mathbf{F} = -\nabla U = \nabla\left(\frac{1}{2}\mathbf{P} \cdot \mathbf{E}\right) \tag{5}$$

and since fused silica is a linear dielectric we can write

$$\mathbf{F} = \frac{1}{2}\varepsilon_0 \chi_e \nabla(E^2) \tag{6}$$

where ε_0 is the permittivity of free space in F/m and and χ_e is the electric susceptibility of the dielectric. I have calculated force profiles for both equations (3) and (6) and they match exactly, as can be seen in figure 9.

The next step of my project was projecting the force profile into each of the modes. We approximate the suspended disk for ease of calculation by discretizing it into a regular, fine grid. The characteristic equation of motion for this system is

$$\hat{M}\ddot{\vec{x}} = -\hat{k}\vec{x} + \vec{f}(t) \tag{7}$$

where $\hat{M}$ is the mass distribution matrix, $\vec{x}$ is a high dimensional vector describing the displacement of each unit of the disk, $\hat{k}$ is the elasticity of the disk, and $\vec{f}$ is the electrostatic force from the ESD. It is useful to note that $\hat{M}$ is diagonal and $\hat{k}$ is symmetric due to the disk's uniform density. We first solve the homogeneous equation

$$\ddot{\vec{x}} = -\hat{M}^{-1}\hat{k}\vec{x}$$

which, in the frequency domain, yields

$$\ddot{\vec{x}} = -\omega^2\vec{x} = -\hat{M}^{-1}\hat{k}\vec{x}. \tag{8}$$

Substituting (8) into equation (7) and rearranging yields

$$\left[-\omega^2\hat{I} + \hat{M}^{-1}\hat{k}\right]\vec{x} = \hat{M}^{-1}\vec{f}. \tag{9}$$

Since (7) is separable we can decompose $\vec{x}$ as

$$\vec{x} = \sum_i^{\infty} \alpha_i(t)\vec{x}_i \tag{10}$$

where each $\vec{x}_i$ is an eigenmode of the system with a corresponding eigenfrequency ω_i. Substituting equation (10) into (9), multiplying by a generalized eigenmode $\vec{x}_j$ and defining $\odot$ to be element-wise multiplication gives us

$$\int \vec{x}_j \odot \sum_i \left[\ddot{\alpha}_i + \omega_i^2 \alpha_i\right] \vec{x}_i \, dV = \int \hat{M}^{-1} \vec{f}(t) \odot \vec{x}_j \, dV. \tag{11}$$

Rearranging (11), we are left with

$$\sum_i \left(\ddot{\alpha}_i + \omega_i^2 \alpha_i\right) \int \vec{x}_j \odot \vec{x}_i \, dV = \int \hat{M}^{-1} \vec{x}_j \odot \vec{f} \, dV. \tag{12}$$

Another important property is the orthogonality of the eigenmodes. This can be seen by multiplying (8) by an eigenmode and integrating as we did in (12) to get

$$\int \vec{x}_j \odot (\hat{M}^{-1} \hat{k} \vec{x}_i) dV = \omega_i^2 \int \vec{x}_j \odot \vec{x}_i dV. \tag{13}$$

Since i and j are arbitrary indices we can switch them and then subtract the two equations to obtain

$$(\omega_i^2 - \omega_j^2) \int \vec{x}_i \odot \vec{x}_j dV = \int \left(\vec{x}_i \odot \hat{M}^{-1} \hat{k} \vec{x}_j - \vec{x}_j \odot \hat{M}^{-1} \hat{k} \vec{x}_i\right) dV \tag{14}$$

Due to the symmetric nature of $\hat{M}^{-1}\hat{k}$, the right hand side of (14) is always zero which indicates that the eigenmodes are linearly independent. Thus it is useful to note that

$$\int \vec{x}_i \odot \vec{x}_j \, dV$$

can be thought of as a normalization constant $m_i \delta_{ij}$ where

$$m_i = \int \vec{x}_i \odot \vec{x}_i \, dV. \tag{15}$$

Therefore, each element of the integrand on the right hand side of equation (12) can be viewed as a normalized projected force profile for any give mode $\vec{x}_j$. By multiplying each mode shape by the force profile and modal mass element-wise and integrating, I was able to calculate a normalized modal force distribution. For the sake of time remaining in the summer I abandoned exact physical units and studied the relative magnitudes of the force without normalizing for the density of the disk. With this framework, I wrote MATLAB scripts to iteratively solve my COMSOL model for various parameters, compute each modal force profile, and then plot the change in modal force with the change in parameter. Thus we were able to determine the optimal values for each of the geometric parameters for the ESD.

Each mode has a doublet where the nodes and anti-nodes are switched as in figure 10. Therefore in order to effectively understand the force distribution for each frequency, both mode shapes must be accounted for. However as in figure 10, one of the modes has a node in the middle of the ESD region where the force is greatest, minimizing the coupling between the force and the resultant vibrational displacement. This effect leads to one of the pair receiving much more force than the

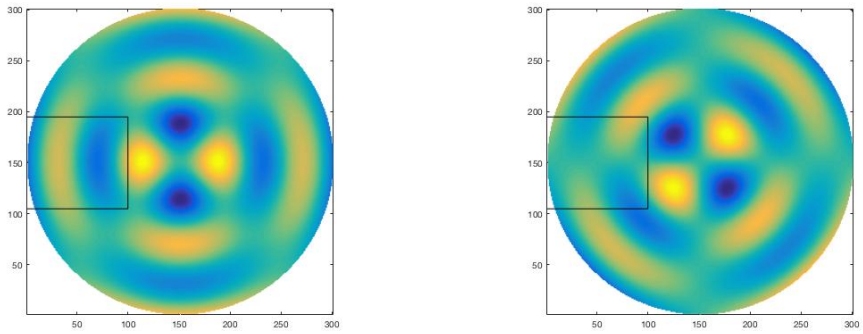

Figure 10: Mode 25 (3,2) and its twin within the doublet, the rectangle outlines the ESD

other. Due to this effect I plotted the larger of the two forces for any given frequency. Mathematically speaking, the force profile is calculated by a spatial integral and the functions that describe the mode doublets are even and odd functions. Thus there will be a point at which the function is even and the integration domain is symmetric relative to the mode function, thus the force will cancel to zero for one and be at a maximum for its doublet. This effect can be easily visualized in the second image in figure 10, the area of the regions of positive and negative displacement within the box denoting the ESD force profile are almost exactly equal. When summing to get the force profile for that mode, the positive and negative regions will almost exactly cancel out leading to almost no force being coupled into that mode.

The important adjustable geometric parameters in the ESD can be seen in figure 5, the only parameter not shown is the vertical distance between the drive and the sample. The results of four of the sweeps can be seen in figures 11-14. Increasing the vertical distance appears to cause the force to drop off proportionally to $\frac{1}{distance^2}$ as in figure 11. When increasing the gap between the arms of the actuator as in figure 12, the lower frequency modes increase and level off around a gap of 1.2 mm with no obvious trend in the higher order modes. There are a couple modes with unique, sharp behavior, part of this is a result of the fact that the force is calculated as an absolute value. If the trend of the force profile crosses the x-axis, the absolute value function reflects it to be positive creating a sharp change in the plot's behavior. Since only the magnitude of the force is important, we want to avoid geometries where the force is 0, but negative forces are perfectly acceptable. The offset sweep in figure 13 is especially interesting, as the offset increases, the force in the higher modes increases by as much as a factor of 6 while the lower modes decrease by no more than 20%. This is likely a result of the fact that increasing the offset narrows the force profile in the disk which leads to more significant coupling into the higher modes with narrower anti-nodes. The final sweep worth analyzing is the widths of the electrode arms in figure 14. There appears to be a linear relationship to the increase in arm width and the resulting force in almost all of the modes. Similar to the gap between the arms, mode 25 has a unique behavior. In the first image of figure 10, the ESD covers two opposite anti-nodes, thus there is a point where the force coupled at each of those points is equal leading to a zero point in the profile. Based on the sweeps I have completed, the optimal parameters are presented in table 2.

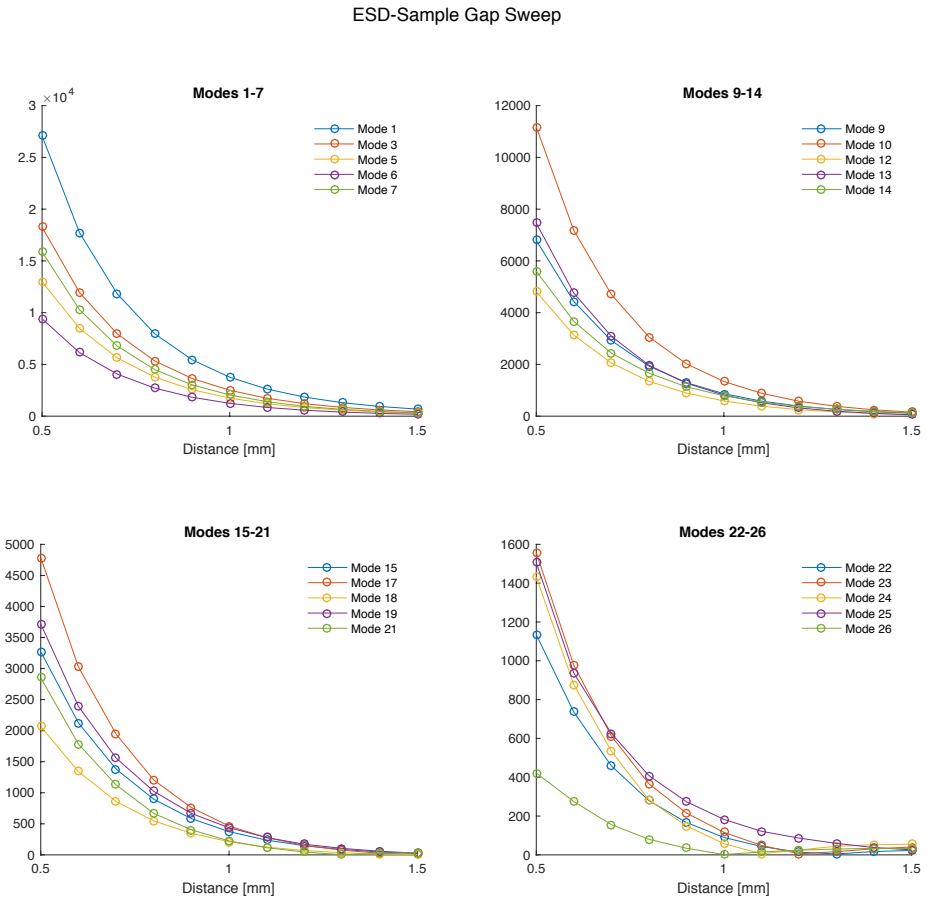

Figure 11: The results of a parametric sweep of the gap between the ESD and the sample. It is important to note that the y-axis units are not physical

Parameter	**Value**
Arm Width	0.55 mm
Gap	0.5 mm
Offset	3.5 mm
Arm Gap	1.25 mm
Arm Length	16 mm

Table 2: Optimized parameters for the original ESD geometry, these parameters improved the design but not enough to be worth manufacturing

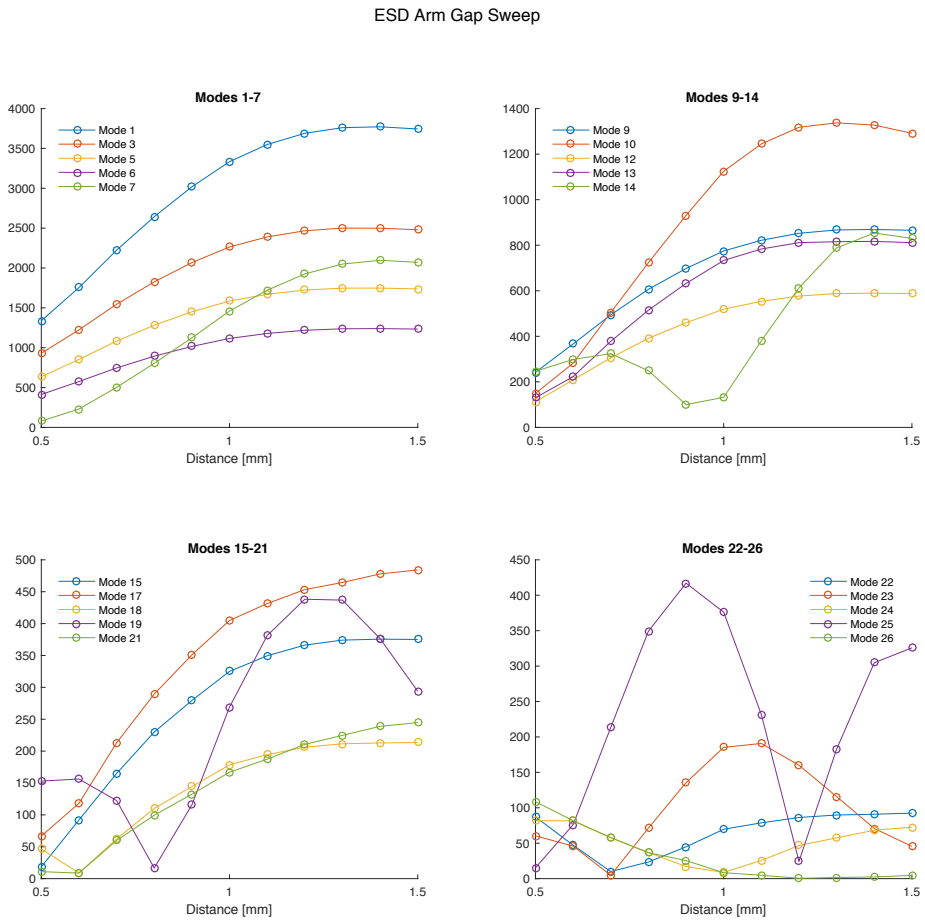

Figure 12: The results of a parametric sweep of the gap between the arms of the ESD, the sharp changes in the trends appear because the results are plotted as an absolute value of the force

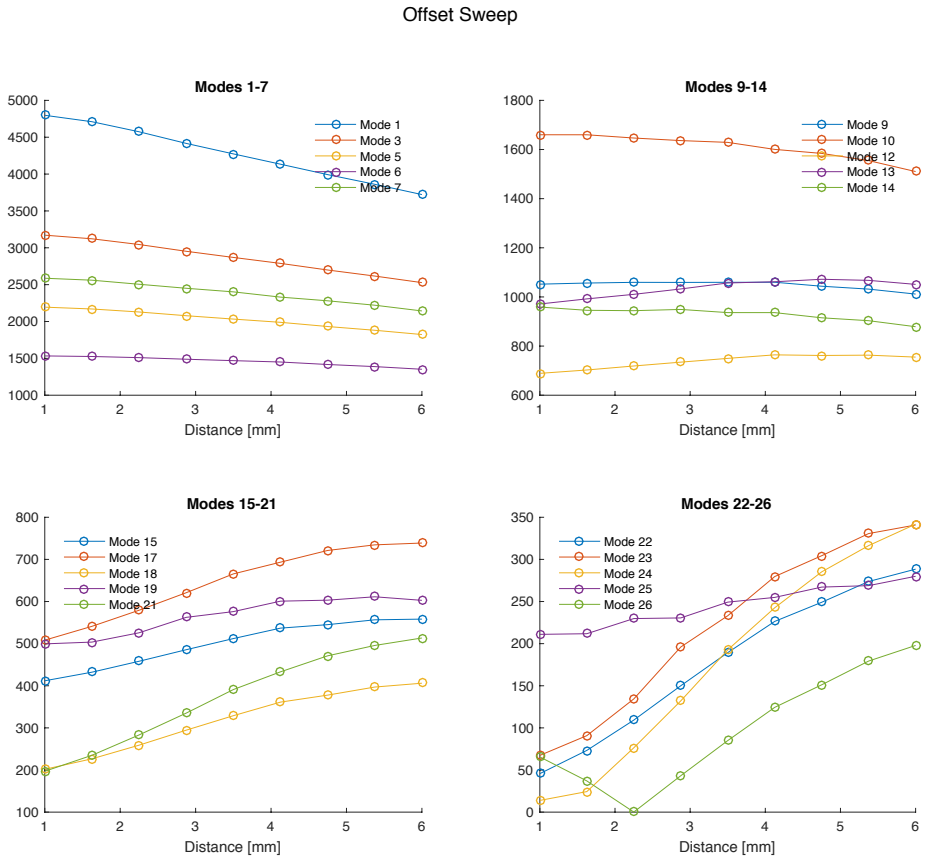

Figure 13: The results of a sweep of the gap between the two combos of the ESD, measured between the end of the arms of one comb and the perpendicular base of the opposite comb. See figure 5 for a visual depiction

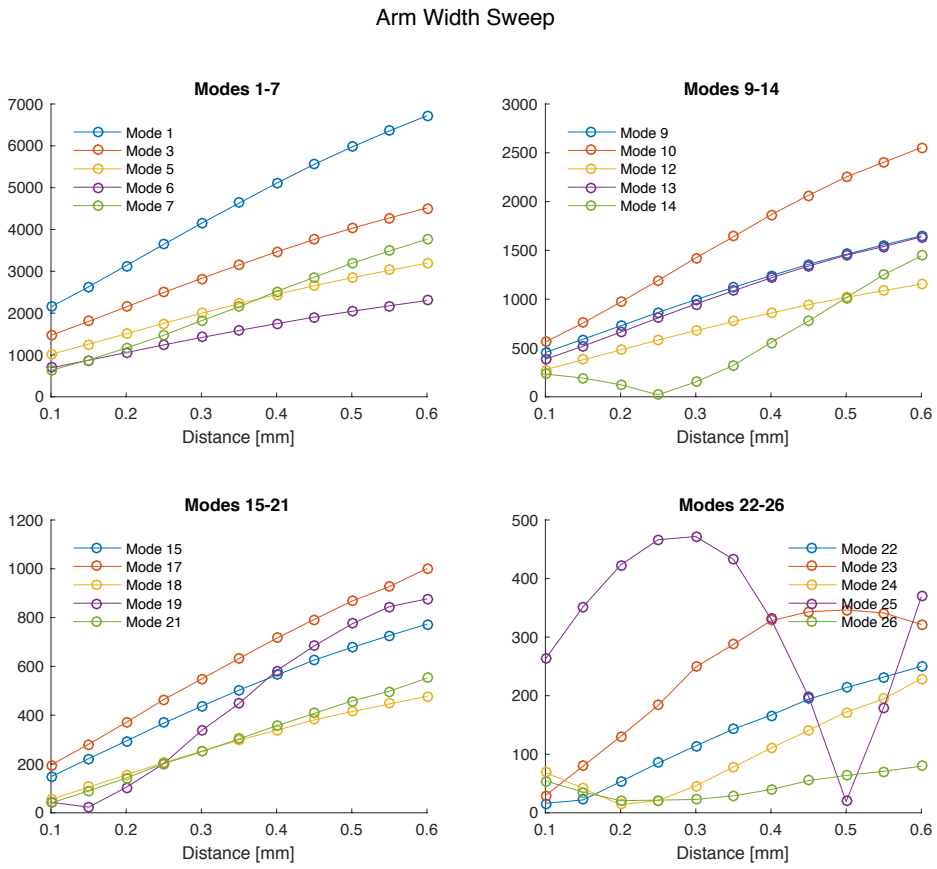

Figure 14: The results of a sweep of the width of the arms of ESD, once again the sharp changes in the trends come from the fact that the sweep is plotted as an absolute value

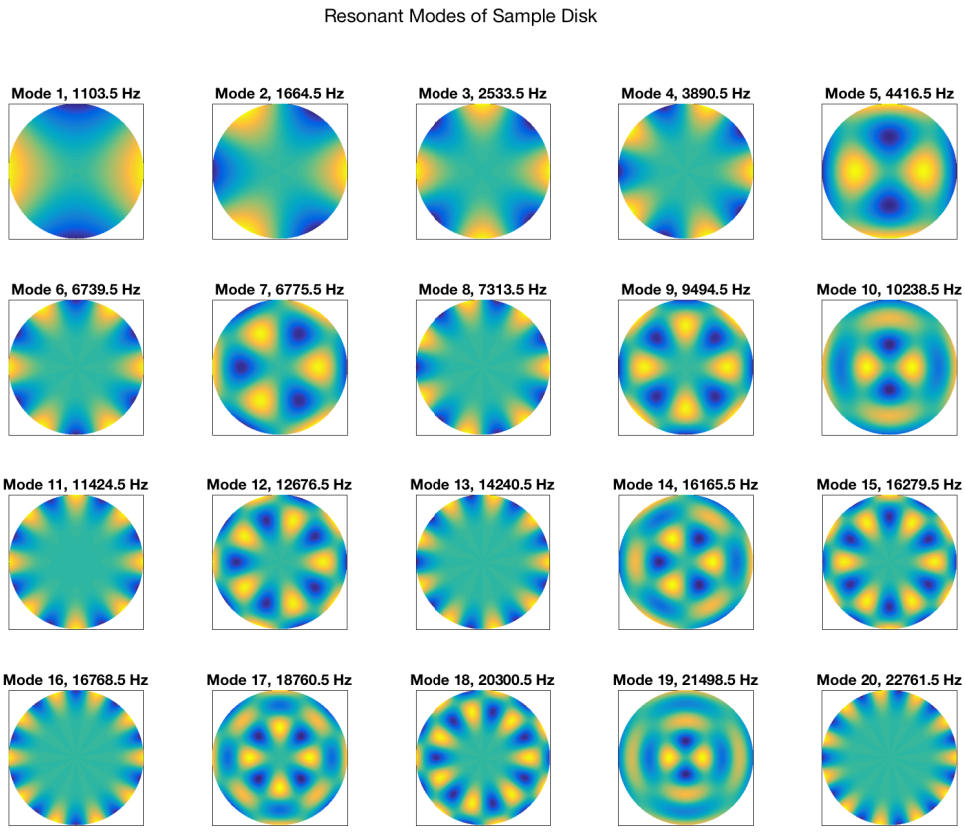

Figure 15: The 20 resonant modes tracked by the C.Ri.Me setup

From these sweeps, the most significant improvement came from minimizing the gap between the ESD and the sample. As a result we tried to place the original ESD closer to the sample in the hope of improving excitation without having to order a brand new drive. This proved logistically difficult and once it was accomplished, some additional effects damped out the improved excitation. It is currently unclear exactly what caused this damping, perhaps a thin layer of air was trapped between the ESD and the sample or the sample lightly touched the ESD. Thus more creative designs became necessary. I tried a variety of alternate designs as can be seen in figures 16a-16d. Most of the designs were quite unsuccessful in simulation, but the two ESD design in figure 16d showed promise. The advantage of the separated design is that it creates two regions of force near the anti-nodes of most of the resonant modes without creating zero crossings. As a result the outer drive position is straightforward, it just needs to be along the edge of the disk. However the inner drive is not so obvious since the modes with multiple radial nodes have anti-nodes at different radial positions. As such, the inner ESD position needs to be determined numerically.

I ran a sweep of the position of the central ESD, as can be seen in the sweep plot in figure 17. The limited range of the sweep was due to time constraints so that the drive could be ordered in time. It is important to note that this sweep is plotted as a ratio to the force profile of the original data. The optimal position is not visually obvious from the sweep plot, so I also plotted the root mean square of the modes that change the most over the course of the sweep. From this, I determined that the optimal position for the central ESD was one shifted 2 mm outward from my original design depicted in figure 16d. The technical drawing for this design can be seen in figure 18. Unfortunately, in a rush to get the design out for fabrication in time we designed it backwards, the two combs of electrodes should be switched relative to the mounting holes and solder pads. The PCB can be seen in figure 19.

Given time and cost restrictions we attempted to mount the reversed ESD in a creative manner so that it could still be usable. We mounted the new ESD to an old one in order to reverse its position relative to the sample, as can be seen in figure 20. We then used the new ESD to measure the Q factors for a disk that had been previously studied with the original model for comparison. Unfortunately the new model did not substantially improve the initial excitation, as is apparent in figure 21. The excitation of my design is more consistent across the modes and a few of the modes did substantially increase, specifically one of the modes near 7 kHz, the mode just above 10 kHz and the mode at around 22 kHz. The substantial losses were the other mode near 7 kHz, the mode at around 9 kHz and the mode at 25 kHz.

3 Conclusions and Further Work

While it is disappointing that my double ESD design did not substantially improve the initial excitation, there are interesting results to be gleaned from my work. The ESD provides a similar excitation with a much smaller force profile than the original design, so its efficiency is certainly improved. Additionally, we learned that the force magnitude is highly dependent on distance from the drive to the sample so perhaps our improvised mounting scheme is placing the drive further away from the sample. Another potential reason for the reduction in force is the flexibility of

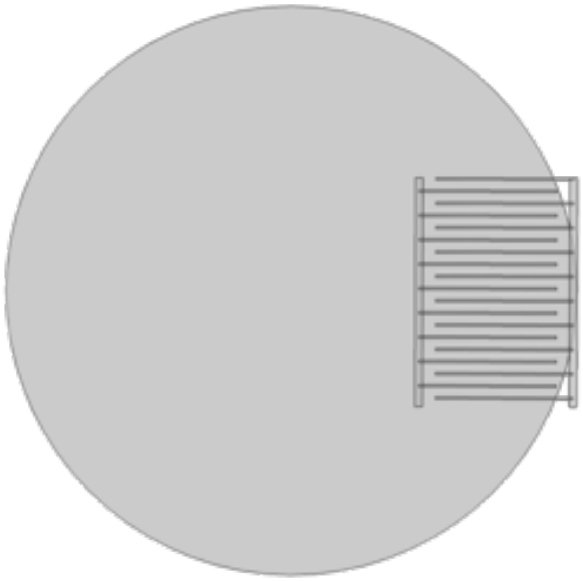

(a) Rotated ESD Design

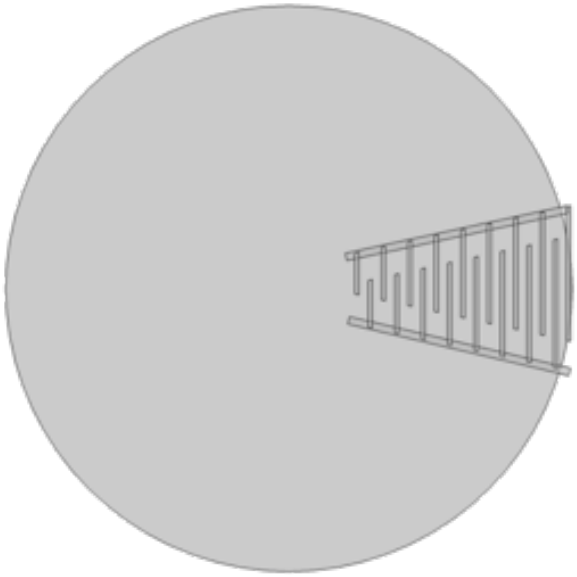

(b) Triangular ESD Design

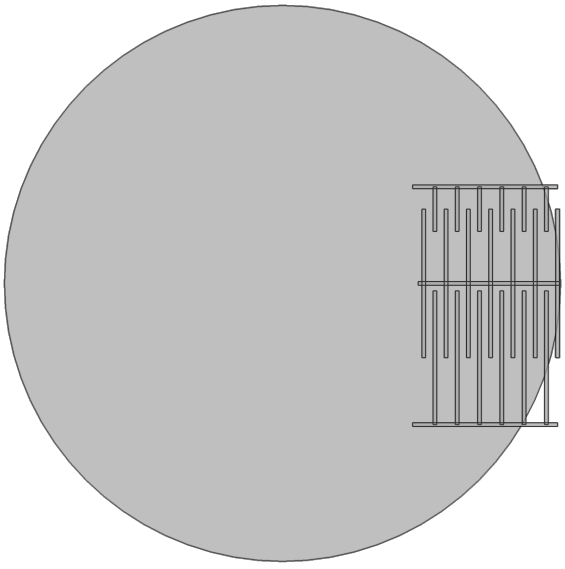

(c) Doubled ESD Design

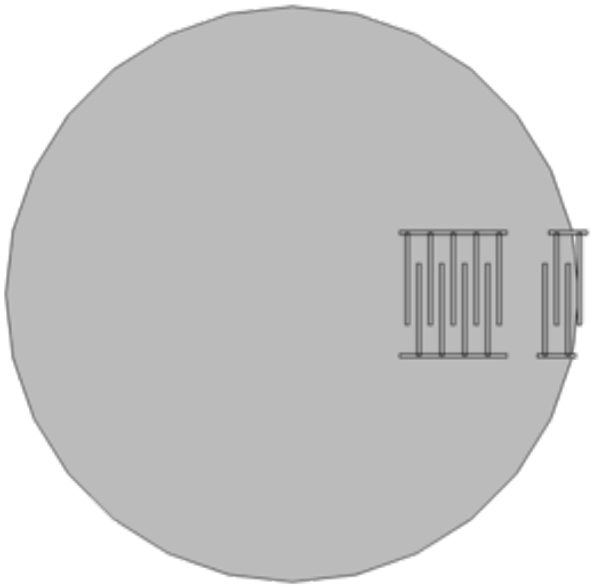

(d) Two ESD Design

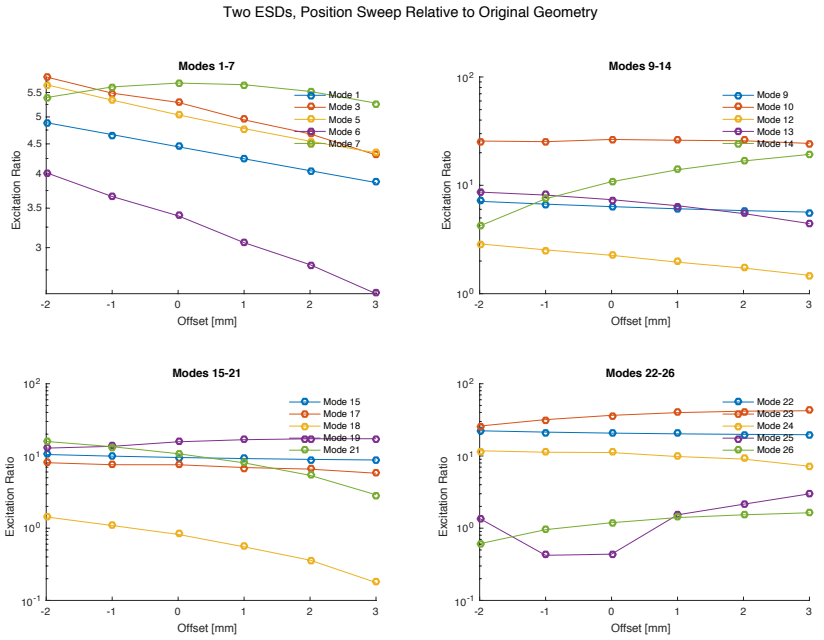

Figure 17: Sweep of the central ESD position

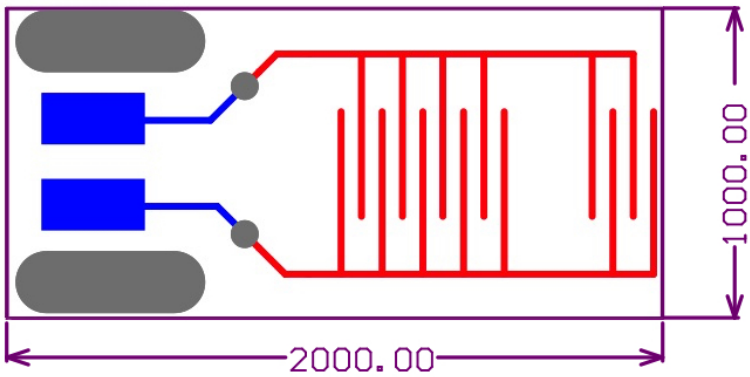

Figure 18: Technical drawing of my optimized ESD design

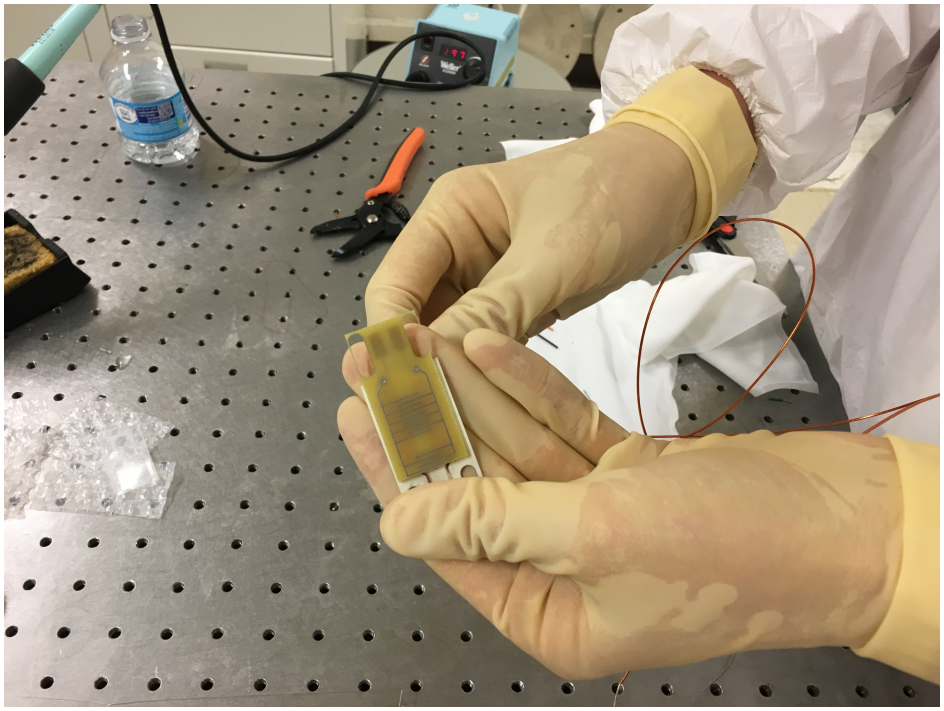

Figure 19: The PCB of my ESD design

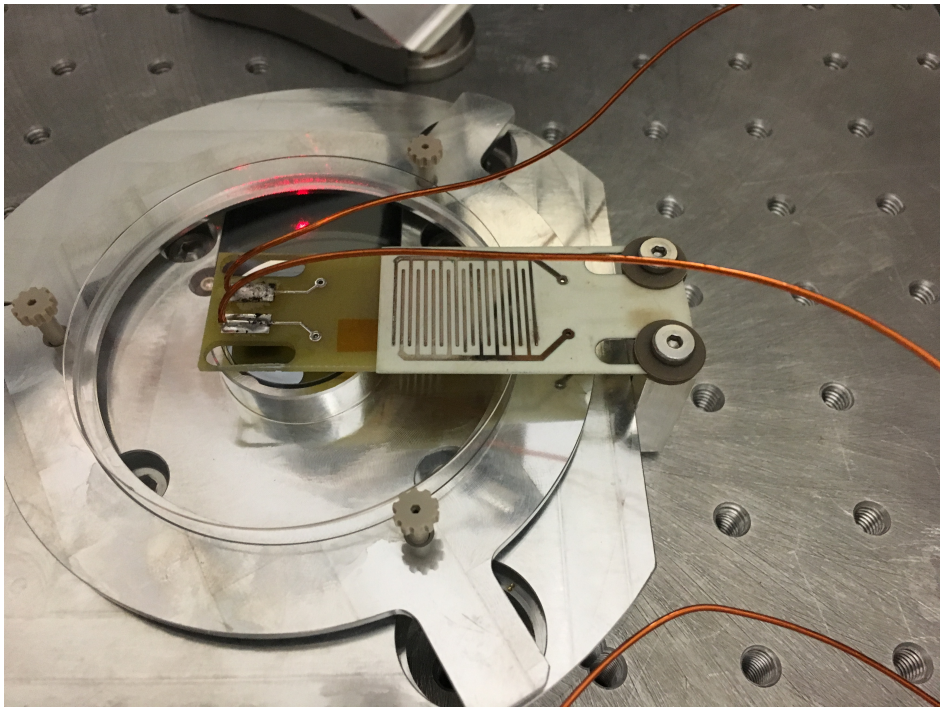

Figure 20: The modified installation method into the vacuum chamber

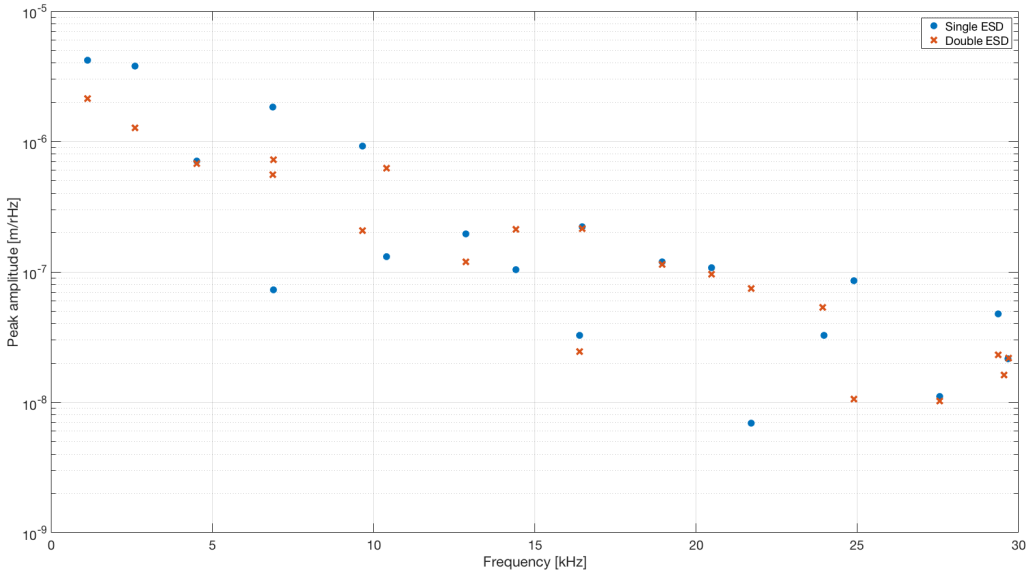

Figure 21: The initial excitation data comparing the original design and my doubled design, there is almost no improvement in the excitation overall

the improvised mounting scheme. Since the ESD is taped to another PCB that is mounted to the apparatus the ESD is quite flexible and it is possible that some of the force is coupled into motion of the ESD. I also developed an effective method to test and optimize additional ESD designs using MATLAB scripts and parametric sweeps.

From this, there is further work to be done. First, determining the reason for the lack of improvement is very important. If I can find an error in my simulations or calculations then I may be able to come up with a design that gives the desired improvements. The first step to doing this is to calculate the excitation from my COMSOL models in physical units that can be compared to real values. I also had very little time to optimize the two drive design because of time restrictions, as such there are multiple geometric parameters of the drive itself that could potentially be improved. If there is not substantial new information to be gleaned from that work, then perhaps ordering a new drive that can be properly mounted would help improve control over the sample gap and therefore improve excitation.

References

[1] E. Cesarini, M. Lorenzini, D. Campagna, F. Martelli, F. Piergiovanni, F. Vetrano, G. Losurdo, G. Cagnoli, "A 'gentle' nodal suspension for measurements of the acoustic attenuation in materials", Review of Scientific Instruments 80, 053904 (2009).

[2] A. Cadez, A. Abramovici, "Measuring high mechanical quality factors of bodies made of bare insulating materials", J. Phys. E: Sci. Instrum. 21 453 (1987).

[3] G. Vajente, A. Ananyeva, G. Billingsley, A. Heptonstall, E. Sanches, C. Torrie, E. Gustafson, R. Adhikari, "CRIME: Coating Ringdown Measurement Experiment", LIGO-G1700348.

[4] G. Vajente, A. Ananyeva, G. Billingsley, A. Heptonstall, E. Sanches, C. Torrie, E. Gustafson, R. Adhikari, "From Q to ϕ", LIGO-G1700349

[5] G. Vajente, "Making C.Ri.Me. Pay: the Coatng Ringdown Measurement Experiment" LIGO-G1700052-v1

[6] D. Griffiths, "Introduction to Electrodynamics", Prentice Hall, (2012).

[7] J. Jackson, "Classical Electrodynamics", Wiley, (1998).

[8] G. Vajente, Technical Drawings, LIGO-D1600197-v4, LIGO-D1600203-v1, LIGO-D1600208-v3, LIGO-D1600276-v1